

Thermal properties of light nuclei from $^{12}\text{C}+^{12}\text{C}$ fusion-evaporation reactions

L Morelli¹, G Baiocco^{1,2} ‡, M D'Agostino¹, F Gulminelli²,
M Bruno¹, U Abbondanno³, S Appannababu⁴, S Barlini^{5,6},
M Bini^{5,6}, G Casini⁶, M Cinausero⁴, M Degerlier⁷,
D Fabris⁸, N Gelli⁶, F Gramegna⁴, V L Kravchuk^{4,9},
T Marchi⁴, A Olmi⁶, G Pasquali^{5,6}, S Piantelli⁶, S Valdré^{5,6}
and Ad R Raduta¹⁰

¹Dipartimento di Fisica ed Astronomia dell'Università and INFN, Bologna, Italy

²LPC (IN2P3-CNRS/Ensicaen et Université), F-14076 Caen cédex, France

³INFN Trieste, Italy

⁴INFN, Laboratori Nazionali di Legnaro, Italy

⁵Dipartimento di Fisica ed Astronomia dell'Università, Firenze, Italy

⁶INFN Firenze, Italy

⁷ University of Nevsehir, Science and Art Faculty, Physics Department, Nevsehir, Turkey

⁸INFN, Padova, Italy

⁹National Research Center "Kurchatov Institute", Moscow, Russia

¹⁰NIPNE, Bucharest-Magurele, POB-MG6, Romania

E-mail: luca.morelli@bo.infn.it

Abstract. The $^{12}\text{C}+^{12}\text{C}$ reaction at 95 MeV has been studied through the complete charge identification of its products by means of the GARFIELD+RCo experimental set-up at INFN Laboratori Nazionali di Legnaro (LNL). In this paper, the first of a series of two, a comparison to a dedicated Hauser-Feshbach calculation allows to select a set of dissipative events which corresponds, to a large extent, to the statistical evaporation of highly excited ^{24}Mg . Information on the isotopic distribution of the evaporation residues in coincidence with their complete evaporation chain is also extracted. The set of data puts strong constraints on the behaviour of the level density of light nuclei above the threshold for particle emission. In particular, a fast increase of the level density parameter with excitation energy is supported by the data. Residual deviations from a statistical behaviour are seen in two specific channels, and tentatively associated with a contamination from direct reactions and/or α -clustering effects. These channels are studied in further details in the second paper of the series.

PACS numbers: 25.70.z, 24.60.Dr, 27.30.+t, 24.10.Pa

NUCLEAR REACTIONS $^{12}\text{C}(^{12}\text{C},X)$, $E = 95$ AMeV, Measured Fusion-evaporation reactions, Observed deviation from statistical behaviour.

Submitted to: *J. Phys. G: Nucl. Phys.*

1. Introduction

The statistical theory of Compound Nucleus (CN) decay is one of the oldest achievements of nuclear physics and has proved its remarkable predictive power since sixty years [1]. Within this theory the detailed output of a generic nuclear reaction is uniquely predicted under the knowledge of nuclear ground state properties and level densities. The knowledge of level densities is not only important for the understanding of nuclear structure [2], but it is also required for different applications of nuclear physics, from nucleosynthesis calculations to reactor science. Its direct measurement from transfer reactions [3] is limited to a relatively low excitation energy domain. Above the thresholds for particle decay, level densities are only accessible in evaporation reactions through the theory of CN decay.

Despite the interest of the issue, mainly inclusive experiments have been used up to now to constrain this fundamental quantity [4], and very few studies exist altogether concerning the evaporation of very light nuclei in the mass region $A \approx 20$ [5, 6, 7]. However, this mass region is very interesting to explore. Indeed some excited states of different nuclei in this mass region are known to present pronounced cluster structures. These correlations may persist in the ground state along some selected isotopic chains [8], and according to the Ikeda diagrams [9] alpha-clustered excited states are massively expected at high excitation energies close to the multi-alpha decay threshold in all even-even $N = Z$ nuclei. These cluster structures have been evidenced in constrained density functional calculations [10, 11, 12] close to the threshold energy of breakup into constituent clusters and even beyond. They should lead to exotic non-statistical decays with a privileged break-up into the cluster constituents which start to be identified in the recent literature [13, 14].

Such effects might be experimentally seen as an excess of cluster production with respect to the prediction of the statistical model, provided that the ingredients of the latter are sufficiently constrained via experimental data. It is important to recall that the final inclusive yields represent integrated contributions over the whole evaporation chain. Because of that, the information they bear on specific excitation energy regions of the different nuclei explored during the evaporation process may be model dependent [15] unless the decay chain is fully controlled in a coincidence experiment. To progress on these issues, we have performed an exclusive and complete detection of the different decay products emitted in $^{12}\text{C}+^{12}\text{C}$ dissipative reactions at 95 MeV. We compared the experimental data to the results of a dedicated Hauser-Feshbach code for the evaporation of light systems (HF ℓ from now on) with transmission coefficients and level densities optimized in the $A \approx 20$ region [16, 17].

In this paper, the first of a series of two, we show that all the observables of dissipative events are fully compatible with a standard statistical behaviour, with the exception of α -yields in coincidence with Carbon and Oxygen residues.

The good reproduction of a large set of inclusive and exclusive observables by the statistical model allows to constrain the least known part of the theory, namely the

behaviour of the level density at high excitation energy, well above the threshold of particle decay. We will show that a fast increase of the level density parameter in the $A \approx 20$ mass region from $a \approx 2.4 \text{ MeV}^{-1}$ at the neutron separation energy, to $a \approx 3.5 \text{ MeV}^{-1}$ at $E^*/A \approx 3 \text{ MeV}$ is compatible with our data.

The observed residual anomalies are tentatively attributed to clustering effects which appear to survive even in the most dissipative events. These effects will be studied in greater detail in the second paper of this series.

2. The statistical decay code

In this section we give the main features of the Monte Carlo HF ℓ statistical decay code. For further details, see [16].

The evaporation of light particles is treated with the standard Hauser-Feshbach (HF) formalism of CN decay [18], with n, p, d, t, ^3He , α particles and ^6Li , ^7Li emission channels included. The expression for the decay width in channel ξ for a hot nucleus (A, Z) excited in its state C (specified by the energy E^* and the angular momentum J), in the framework of the HF model reads:

$$\Gamma_{\xi}^C = \frac{1}{2\pi\rho_C} \int_0^{E^*-Q} d\epsilon_{\xi} \sum_{J_d} \sum_{j=|J-J_d|}^{J+J_d} \sum_{\ell=|j-s_p|}^{j+s_p} T_{j,s_p}^J(\epsilon_{\xi}) \rho_d \quad (1)$$

where ϵ_{ξ} is the relative kinetic energy of the decay products (the daughter nucleus, labeled by d , and the evaporated particle, labeled by p); Q is the decay Q -value; J_d , s_p and ℓ are the angular momentum of the daughter nucleus, the spin of the evaporated particle and the orbital angular momentum of the decay, respectively and summations include all angular momentum couplings between the initial and final states; T is the transmission coefficient; $\rho_C(E^*, J)$ and $\rho_d(E^* - Q - \epsilon_{\xi}, J_d)$ are the nuclear Level Density (LD) of the decaying and of the residual nucleus, respectively.

The widths Γ_i^C are calculated for all possible decay channels and the Branching Ratio (BR) associated with a specific channel ξ is obtained as the ratio between Γ_{ξ}^C and the total decay width for the hot nucleus: $BR^C(\xi) = \Gamma_{\xi}^C / \sum_i \Gamma_i^C$. This decay probability constitutes the main ingredient of the Monte Carlo simulation.

In the case of the very light CN studied in this work, simple analytical expressions can be safely employed for the transmission coefficients. In our code we have adopted the empirical work of [19]:

$$T_{\ell}(\epsilon_{\xi}) = \frac{1}{1 + \exp\left(\frac{V_b - \epsilon_{\xi}}{\delta \cdot V_b}\right)} \quad (2)$$

where the barrier V_b is a sum of a Coulomb and a centrifugal term depending on ℓ , hence on all coupled angular momenta, see (1). Its full expression reads:

$$V_b = \frac{1.44}{a} \frac{Z_p(Z - Z_p)}{(A - A_p)^{1/2} + A^{1/3}} + \frac{\hbar^2 \ell(\ell + 1)}{2m^2} \frac{\frac{A}{A_p(A - A_p)}}{\left[\frac{A - A_p}{A} \right]^{1/2} + \left[\frac{A - A_p}{A} \right]^{1/3}}^2$$

The two free parameters δ and r_Z were optimized to reproduce the decay of discrete resonances [19]. They depend on the charge Z_p of the evaporated particle, and δ also depends on whether the emission takes place in the sub- or above-barrier region.

Concerning the kinematics of the decay with angular momentum, we have adopted the semi-classical approach proposed by the GEMINI code [20]. Angular momenta are considered as classical vectors, and \mathbf{j}_a and \mathbf{j}_b are coupled under the assumption of equiprobability for the module of their sum \mathbf{j}_s between $|\mathbf{j}_a - \mathbf{j}_b| \leq \mathbf{j}_s \leq |\mathbf{j}_a + \mathbf{j}_b|$. Once the decay channel has been selected, the angular momentum J_d is obtained through a maximization of $\rho_d(J)$ as a function of J . Decay Q -values are calculated from experimental binding energies taken from the Audi and Wapstra compilation [21]. Finally, a special effort has been devoted to the implementation of the level density model. In particular, all information on measured excited levels from the online archive NUDAT2 [22] has been explicitly and coherently included in the decay calculation.

2.1. The level density model

The back-shifted Fermi gas model (BSFG), with the level density parameter and the pairing backshift left as free fit parameters, is known to be a phenomenological approach well suited to reproduce the many-body correlated nuclear level density: pairing effects are included through the backshift Δ_p , and all correlations are taken into account in the renormalization of the LD parameter $a(E^*)$.

In [7] level density parameters for the BSFG model have been determined for a large set of nuclei (310 nuclei between ^{18}F and ^{251}Cf), by the fit of complete level schemes at low excitation energy and s -wave neutron resonance spacings at the neutron binding energy.

In [7], the adopted expression for $\rho(E^*)$ (after integration on angular momentum J and parity π) reads:

$$\rho(E^*) = \frac{\exp[2\sqrt{a(E^* - E_2)}]}{12\sqrt{2}\sigma a^{1/4}(E^* - E_2)^{5/4}} \quad (3)$$

where σ is the spin cut-off parameter:

$$\sigma^2 = 0.0146A^{5/3} \frac{1 + \sqrt{1 + 4a(E^* - E_2)}}{2a} \quad (4)$$

The energy backshift $\Delta_p = E_2$ is left as the first free parameter in the data fitting. The second fit parameter is the asymptotic value \tilde{a} of the following functional form for $a(E^*, Z, N)$ [23]:

$$a = \tilde{a} \left[1 + \frac{S(Z, N) - \delta E_p}{E^* - E_2} \left(1 - e^{-0.06(E^* - E_2)} \right) \right] \quad (5)$$

where $S(Z, N) = M_{exp}(Z, N) - M_{LD}(Z, N)$ is a shell correction term, M_{exp} and M_{LD} being respectively the experimental mass and the mass calculated with a macroscopic liquid drop formula for the binding energy not including any pairing or shell corrections.

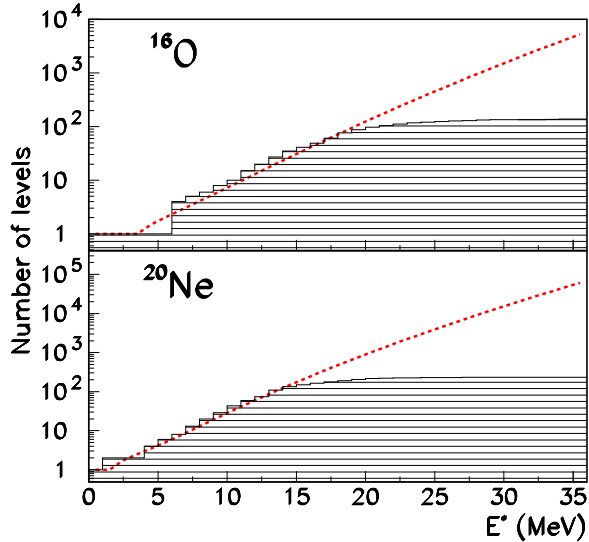


Figure 1. Color online: Comparison between the cumulative number of levels given by (3) (lines), and the cumulative counting of experimentally measured levels from the NUDAT2 archive [22] (histograms).

on the parameter definition and fit procedure can be found in [7]. As a final result, analytic formulas for E_2 and \tilde{a} as a function of tabulated nuclear properties are given. With such formulas for the calculation of LD parameters, the model of (3) allows for a very good reproduction of experimental distributions of measured levels in the mass region of interest for the present work. Two selected examples are given in Figure 1. The isotope ^{20}Ne belongs to the fitted data set, and the good agreement between the line and the histogram shows the quality of the fit procedure of [7]. Concerning ^{16}O , the values of the parameters are an extrapolation of the formulas proposed in [7] out of the fitted data set; from the figure it is also clear that (3) can be considered reliable also for nuclei whose level density has not been directly optimized. A similar agreement is observed for all the other particle-stable isotopes in the mass region of interest for the present study.

Still, numerical values for the pairing backshift and for the asymptotic limit of $a(E^*)$ with increasing excitation energy obtained through this approach are to be considered reliable only up to $E^*/A \approx 1$ MeV for $A \approx 20$ nuclei.

In particular, it is found that the values of the level density parameter needed to reproduce the information on discrete levels are usually lower than the ones coming from higher-energy constraints, through the reproduction of data for fusion-evaporation or evaporation-after fragmentation studies ($E^*/A \approx 2 \div 3$ MeV). A functional form giving a good reproduction of evaporation spectra at very high excitation energy was

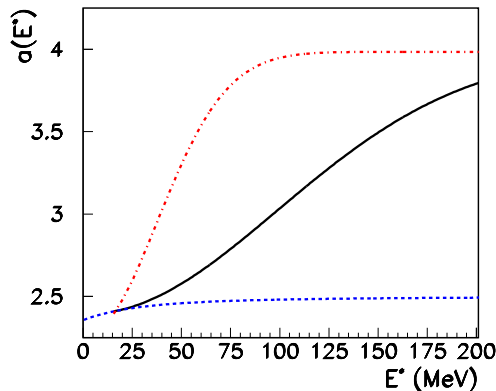


Figure 2. (Colour online) Level density parameter calculation for ^{20}Ne . Blue dashed line: (5). Black solid and red dot-dashed lines: (7) with $E_l = 8$ and 3 AMeV, respectively.

proposed in [24]:

$$a_\infty = \frac{A}{14.6} \left(1 + \frac{3.114}{A^{1/3}} + \frac{5.626}{A^{2/3}} \right) \quad (6)$$

To correctly reproduce at the same time the low- and high-energy experimental constraints, we have adopted a functional form for the level density parameter that gives a continuous interpolation between (5) and (6).

We have adopted the following expression:

$$a(E^*, A) = \begin{cases} a_D = (5) & \text{if } E^* \leq E_m + E_2 \\ a_C = \alpha \exp[-\beta(E^* - E_2)^2] + a_\infty & \text{if } E^* > E_m + E_2 \end{cases} \quad (7)$$

The choice of a rapid (exponential) increase is imposed by the fact that the asymptotic value (6) is connected to the opening of the break-up or multifragmentation channels, which is a sharp threshold phenomenon. The α and β parameters are fully determined by the matching conditions between the low-energy and high-energy regime: $a_D(E_m, A) = a_C(E_m, A)$ and $a_C(E_l, A) = a_\infty \pm 10\%$.

Here, E_l represents the limiting energy at which the break-up or fragmentation regime is attained, while E_m is the excitation energy marking the transition between the discrete and the continuum part of the spectrum. This latter quantity is of the order of $E_m \approx 10$ MeV, coherently with the value of the critical energy for the damping of pairing effects in [25]. In the case of light nuclei for which a large set of measured levels is available, this value well corresponds to the excitation energy maximizing the number of levels in bins of E^* . Above E_m the experimental information is too poor to consider the set of resolved levels exhaustive of the nuclear level density, due to the physical emergence of the continuum.

The limiting energy E_l is then left as the only free parameter of the calculation,

functional form resulting for the level density parameter, in Figure 2 we plot $a(E^*, A)$ for ^{20}Ne , for two different choices of E_l .

In the statistical code, starting from a given CN (A, Z, J, E^*) , the decay pattern is calculated with the Monte-Carlo technique as a sequence of two-body decays governed by the emission probability given by (1). When the emitted particle leaves the daughter nucleus at an excitation energy $E_d^* < E_m$, the excitation energy is considered as a discrete variable, and one of the tabulated levels [22] of the daughter discrete spectrum is populated. The level is chosen according to the Breit-Wigner distribution of the discrete levels considering their respective widths, including the full spectroscopic information of [22], and the particle kinetic energy is adjusted if necessary to ensure energy conservation. When a particle bound level is populated, the subsequent decay is assumed to be due to a single γ emission to the corresponding ground state. If the daughter excitation energy E_d^* is greater than E_m , the spectroscopic information is not sufficient to fully constrain the spin and energy of the daughter nucleus. If measured excited states exist, they are populated with a probability given by the ratio between the measured level density from discrete states and the total level density including the continuum states and given by (3) with a given by (7). If no levels are known, the emission is assumed to take place in the continuum.

3. Experiment and data selection

The measurement was performed in the third experimental Hall of LNL. The $^{12}\text{C}+^{12}\text{C}$ reaction had been already studied in a previous experiment, and first results on the persistence of cluster correlations in dissipative reactions highlighted by the comparison of the data set with HF ℓ calculations were reported [17]. The limited statistics of the experiment prevented detailed studies of the breakup angular and energy correlations. Here we report the analysis of the new data-taking, which confirms our previous findings and additionally allows to study the deviations from statistical behaviour in specific channels and in greater detail.

A pulsed beam (less than 2 ns FWHM, 400 ns repetition period) of ^{12}C provided by the TANDEM accelerator impinged with a self-supporting ^{12}C target, with a thickness of $85 \mu\text{g}/\text{cm}^2$. The bombarding energy was 95 MeV.

3.1. The experimental setup

The experimental setup is composed by the GARFIELD detector, covering almost completely the angular range of polar angles from 30° to 150° , and the Ring-Counter (RCo) annular detector [26], centered at 0° with respect to the beam direction and covering forward laboratory angles in the range $5^\circ \leq \theta \leq 17^\circ$.

The combination of the two devices allows for a nearly- 4π coverage of the solid angle, which, combined with a high granularity, permits to measure the charge, the energy and the emission angles of nearly all charged reaction products. The setup also

provides information on the mass of the emitted charged products in a wide range of particle energy [27].

The GARFIELD apparatus is a two-detection stage device, consisting of two microstrip gaseous drift chambers (μSGC), filled with CF_4 gas at low pressure (50 mbar) and placed back to back, with $\text{CsI}(\text{Tl})$ scintillation detectors lodged in the same gas volume.

Due to the small size of the studied system, mainly light particles are emitted in the reaction which are efficiently detected and identified through the use of the *fast – slow* shape method for the 180 $\text{CsI}(\text{Tl})$ scintillators [28].

The energy identification thresholds result, on average, 3, 6, 9, 20, 7 MeV for p , d , t , ^3He , and α particles, respectively. As for other experimental devices using the *fast – slow* technique [29], ^3He can be discriminated from α 's starting from ≈ 20 MeV. This increase of the ^3He threshold does not affect too much the α yield in our reaction, since ^3He is estimated to represent less than 2-3% of $Z=2$ particles [17]. In all the experimental percentages, the associated error takes into account both the statistical error and the possible $^3\text{He} - \alpha$ contamination. In the present analysis, the information coming from the μSGC has been used to validate the particle identification, especially in the lower part of the range, where the *fast – slow* curves tend to merge.

The RCo detector is an array of three-stage telescopes realized in a truncated cone shape. The first stage is an ionization chamber (IC), the second a $300\mu\text{m}$ reverse mounted Si(nTD) strip detector, and the last a $\text{CsI}(\text{Tl})$ scintillator.

The angular resolution is $\Delta\theta \approx \pm 0.7^\circ$ and the energy resolution of silicon strips and $\text{CsI}(\text{Tl})$ detectors resulted 0.3% and 2-3%, respectively. In the present experiment, reaction products with $Z \geq 3$ have relatively low energies and are stopped in the Si detectors. Therefore, they can be identified only in charge thanks to the $\Delta E - E$ correlation between the energy loss in the gas and the residual energy in the silicon detectors, with 1 AMeV energy threshold. Only for the high energy tails of $3 \leq Z \leq 5$ fragments mass identification has been possible, thanks to the application of a pulse shape technique to signals coming from the Si detectors [30]. Light charged particles (LCP, $Z = 1, 2$) flying at the RCo angles and punching through the $300 \mu\text{m}$ Si pads ($E/A \geq$ about 6 MeV) are identified in charge and mass by the conventional Si - CsI $\Delta E - E$ method. LCP stopped in the silicon stage are identified only in charge.

More details on this setup can be found in [27].

3.2. Minimum bias compound nucleus selection

The analysis considers only events with a coincidence between at least one LCP, detected and identified in GARFIELD, and a particle or fragment ($Z \geq 3$) detected at forward angles in the RCo and identified in charge. In the case of a fusion-evaporation reaction, this latter is the residue Z_{res} of the CN decay chain, and it is expected to have a velocity close to the center-of-mass velocity of the reaction, $v_{CM} \approx 2$ cm/ns. Due to the lack of isotopic resolution for such low energy fragments, a hypothesis on their mass has to be

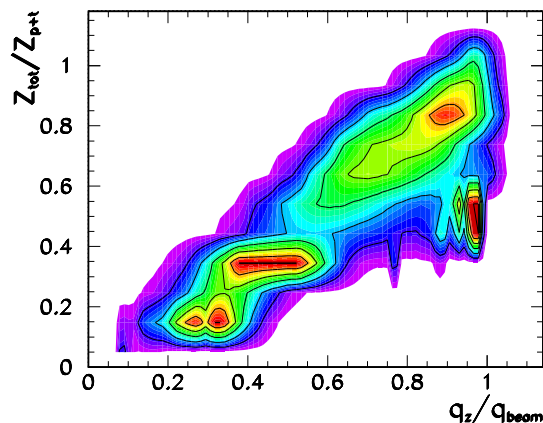


Figure 3. Colour online: Contour plot of the total detected charge (Z_{tot}) normalized to the sum of the projectile and target charge Z_{p+t} as a function of the total measured longitudinal momentum (q_z) normalized to the projectile momentum (q_{beam}).

done. Our initial hypothesis (to be further discussed in §4.2) is $A_{res} = 2 \cdot Z_{res}$.

A first selection within the measured events is based on Figure 3, where we show the total detected charge as a function of the total longitudinal momentum. Requiring that at least 60% of the total incoming parallel momentum is collected, we obtain a total charge distribution centered at $Z_{tot} = 10$, corresponding to the 80% of the total charge. A yield peak around $Z_{tot}/Z_{p+t} = 0.5$ is evident in the picture, corresponding to (quasi)–elastic events with only the Carbon ejectile detected. Since we would like to concentrate on specific decay channels, we would keep a complete detection ($Z_{tot} = 12$). We have therefore checked that this stringent requirement does not bias the characteristics of the events, comparing the distribution of representative observables with a less stringent selection $Z_{tot} \geq 10$. Very similar distributions are obtained with the two “minimum bias” selections which henceforth we name “quasi-complete” ($Z_{tot} \geq 10$) and “complete” ($Z_{tot} = 12$) (see § 4.1). Complete events are $\approx 20\%$ of quasi-complete ones.

4. Data analysis and comparison to statistical model calculations

With the minimum bias event selections discussed in § 3.2, we compare experimental data to the predictions of our Monte Carlo Hauser-Feshbach code HF ℓ (§2) for the evaporation of the CN ^{24}Mg , at $E^*/A_{CN} = 2.6$ MeV, issued in case of complete fusion. The angular momentum input distribution for the fused system in this reaction can be assumed to be a triangular one, with a maximum value $J_{0\ max} = 12 \hbar$, coming from the systematics [31]. Because of parity conservation, only even values of J_0 extracted from the triangular distribution are allowed as an input for the CN angular momentum. Finally, code predictions are filtered through a software replica of the experimental set-up, taking into account the geometry, the energy thresholds, the energy resolution and

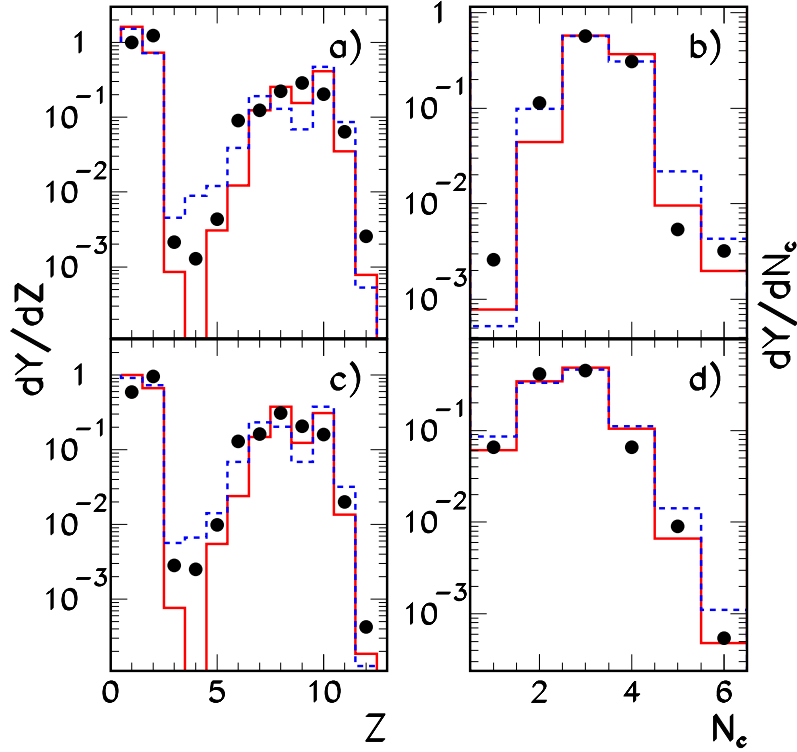


Figure 4. Colour online: Measured (symbols) and calculated (histograms) charge and charged particle multiplicity distribution. Panels a), b) refer to complete ($Z_{tot} = 12$) events, panels c), d) to quasi-complete events ($Z_{tot} \geq 10$). The red solid line gives the result of the HF ℓ calculation, while the blue dashed line is obtained using the GEMINI++ model. All distributions are normalized to the total number of events.

the solid angle for each detector.

The comparison of various experimental and simulated observables is used to validate the parameterizations of statistical model ingredients implemented in the code.

4.1. Experimental observables

The inclusive charge and multiplicity distribution of events completely and quasi-completely detected in charge are presented in Figure 4 in comparison with the filtered HF ℓ calculation. In this figure and in the following ones experimental data are always shown with statistical error bars, when visible.

The charge distribution is globally well-reproduced by the theoretical calculation and its overall shape is typical of fusion-evaporation reactions.

However, a few discrepancies can be observed. Notably, $Z = 4$ fragments are absent in the Hauser-Feshbach prediction while they are not negligible in the experimental sample. This could be interpreted as the presence of a break-up contribution in the data which is not properly treated by the sequential calculation. To confirm this statement,

the same filtering procedure. This model, which has also been largely and successfully used by the nuclear physics community since more than 20 years, includes the emission of intermediate mass fragments within the transition state formalism. We can see that GEMINI++ predicts sizeable yields of the lightest fragments, which in the Hauser-Feshbach formalism have a negligible probability to be emitted and are only obtained as evaporation residues. In particular, the transition state formalism succeeds in explaining the missing Be cross section.

Concerning the multiplicity distribution, presented in the right part of Figure 4, we can see that both the HF ℓ and the GEMINI++ calculations reproduce the data satisfactorily. We can however remark that GEMINI++ overpredicts events of high multiplicity. This means that the transition state formalism is not entirely satisfactory in describing the production of light fragment, which could also be due to a breakup mechanism. Such a mechanism is not accounted for in the presented models.

Apart from the missing $Z = 4$ channel, another discrepancy between the HF ℓ calculation and the data concerns the $Z = 6$ yield which is underestimated by the model. This extra yield could in principle be explained by the transition state model, as shown by the fact that data are well reproduced in this channel by GEMINI++. As an alternative explanation, the Carbon excess with respect to HF ℓ predictions could be due to the entrance channel of the reaction. Indeed, many other experiments [32] where reactions with Carbon projectile and/or target were studied, showed an extra-production of Carbon residues with respect to statistical models expectations. At low bombarding energy, $C-C$ quasi-molecular states [32] can be invoked. In our experiment, as it will be discussed in the following, this anomaly is essentially associated with the specific $C - 3\alpha$ channel.

Because of the great similarity between the HF ℓ and GEMINI++ calculations, and the fact that the HF ℓ code was optimized on light systems (see §2), in the following we exclusively use the HF ℓ code as a reference statistical model calculation.

Due to the low statistics of the experiment for $Z = 3, 4$ residues, we will not study these residue channels any further.

The dominant fusion-evaporation character of the reaction is further demonstrated in Figure 5, which shows the velocity distributions in the laboratory frame of the different fragments with $Z \geq 5$. The good reproduction by the statistical model allows to interpret these fragments mainly as evaporation residues left over by the decay of ^{24}Mg CN originated from complete fusion.

A complementary information is shown in Figure 6, which displays the laboratory energy spectra of protons and α particles detected in GARFIELD. Experimental data (dots) are compared to model calculations (lines). From now on we will concentrate on events with a residue detected in the RCo ($5^\circ \div 17^\circ$) and LCP in GARFIELD ($30^\circ \div 150^\circ$) as in the previous experiment [17]. This choice is essentially due to the different thresholds on LCP identification in RCo and GARFIELD, as pointed out in §3.1. To facilitate the comparison of the spectral shapes, distributions are always normalized to the same area.

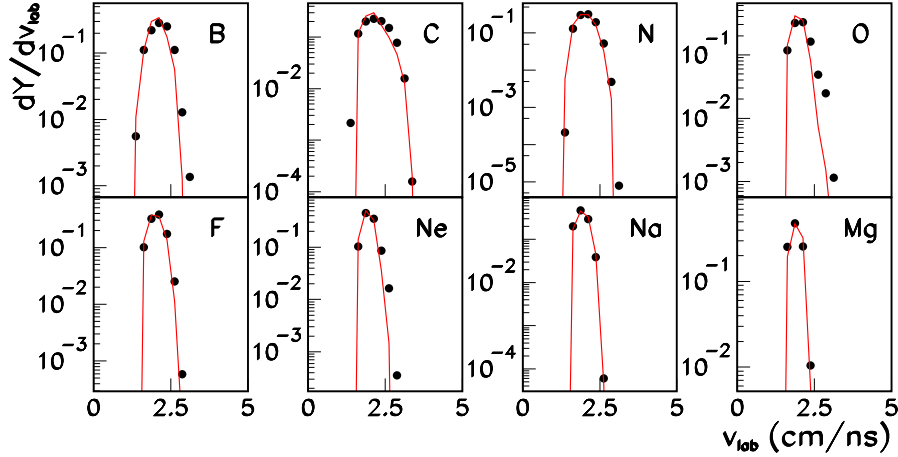


Figure 5. (Colour online) Residue laboratory velocity for complete events ($Z_{tot} = 12$) (symbols) in comparison with the HF ℓ calculation (lines). All distributions are normalized to unitary area.

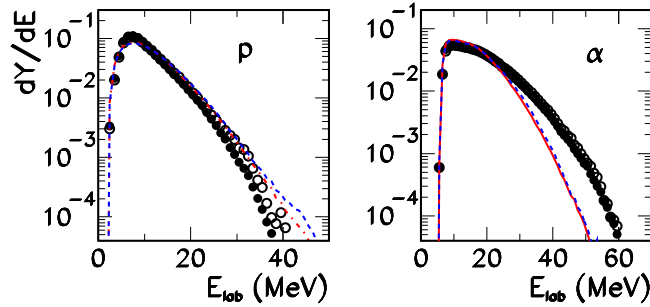


Figure 6. (Colour online) Proton (left part) and α (right part) energy distributions in the laboratory frame, detected in quasi-complete $Z_{tot} \geq 10$ events (full symbols) and in complete $Z_{tot} = 12$ events (open symbols). Data (symbols) are compared to model calculations (lines). Red solid lines: quasi-complete $Z_{tot} \geq 10$ events. Blue dashed lines: complete $Z_{tot} = 12$ events. All spectra are normalized to unitary area.

We can see that the choice of the set of events (complete and quasi-complete) does not deform the shape of the spectra. A satisfactory reproduction of the proton energy spectrum is achieved, while a large discrepancy in the shape of the distributions appears for α particles for both completeness requirements.

Another information can be obtained from angular distributions of protons and α -particles (see Figure 7). The proton distribution is in agreement with the model, while the excess of α particles at backward laboratory angles could suggest a preferential alpha emission from the quasi-target. Alternatively, it could indicate an alpha transfer

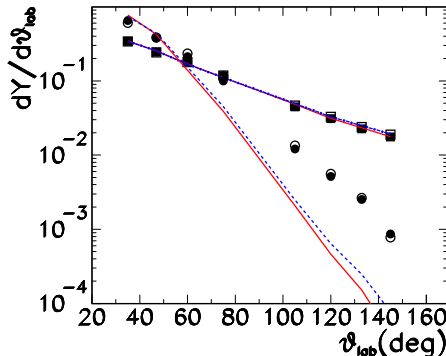


Figure 7. (Colour online) Proton (squares) and α (circles) angular distributions in the laboratory frame, detected in complete $Z_{tot} = 12$ (open symbols) and in quasi-complete $Z_{tot} \geq 10$ (full symbols) events. Data (symbols) are compared to model calculations (lines). Blue dashed lines correspond to complete events, red solid lines to quasi-complete events. Experimental and calculated distributions are normalized to unitary area.

mechanism from an excited ^{12}C nucleus with strong alpha correlations.

As it is commonly known, the shape of LCP energy spectra is determined by the interplay of all physical ingredients entering in the evaporation process, notably including transmission coefficients, angular momentum effects and level density [4]. Nevertheless, when comparing data to statistical model calculations, it is possible to try to disentangle the effects of single ingredients [4]. In particular, while transmission coefficients define the shape of evaporated spectra in the Coulomb barrier region, the level density mostly affects the slope of the exponential tail. Concerning angular momentum, the inclusion of deformation has a stronger influence on heavier fragment emission, as it is the case for α particles, and, as a consequence, the tail of the energy distribution for such fragments becomes steeper.

Thus the two theoretical uncertainties which could be responsible of the observed deviations are the estimated maximum angular momentum leading to CN formation, and the level density parameter. As we have discussed in § 2, the only unknown in the level density is the asymptotic value of the a parameter at very high excitation energy. The effects of a very wide variation of these parameters, including an unrealistically low value of l_{max} and a very high value of E_l are shown in Figure 8. This figure shows that no common choice on the LD parameters can be done in order to reproduce at the same time proton and α energy spectra. For this reason we keep in the rest of the analysis the fiducial values $l_{max} = 12\hbar$, $E_l = 3$ AMeV (red lines).

The comparison made so far on many inclusive observables suggests that the dominant reaction mechanism is CN formation and the discrepancy found for α particles reflects an out-of-equilibrium emission.

A first confirmation of this hypothesis comes from the finding that the largest source

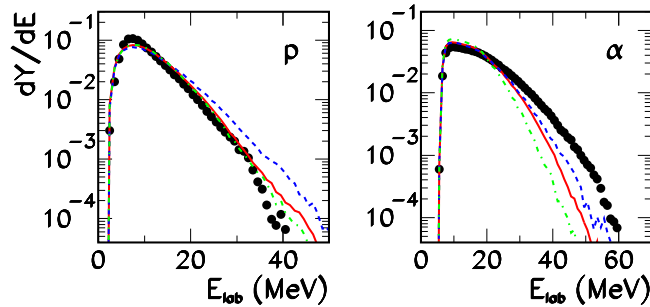


Figure 8. (Colour online) Proton (left part) and α (right part) energy distributions in the laboratory frame, detected in complete events. Data (symbols) are compared to model calculations, with different choices for the assumed maximum angular momentum l_{max} and limiting energy E_l . Red solid lines: $l_{max} = 12\hbar$, $E_l = 3$ A MeV. Blue dashed lines: $l_{max} = 12\hbar$, $E_l = 8$ A MeV. Green dot-dashed lines: $l_{max} = 6\hbar$, $E_l = 3$ A MeV. All spectra are normalized to unitary area.

of disagreement between data and calculations is for decay channels with α particles detected in coincidence with an Oxygen fragment. This is shown in Figure 9, which presents energy spectra of protons and α particles detected in coincidence with a residue of a given atomic number. The discrepancy, larger at the most forward angles [16], is mainly due to the 2 α -channel, as we will discuss in § 4.3.

With the exception of the $\alpha - O$ coincidence, particle energy spectra are very well reproduced by the statistical model. This gives strong confidence to our level density model of (3) and (7) with $E_l = 3$ A MeV (corresponding to $a \approx 3.5$ MeV $^{-1}$ for $E^*/A = 3$ MeV) for the light $A \approx 20$ CN decay.

A small difference of the experimental and calculated energy spectra is also observed for α -particles in coincidence with a Carbon residue. This does not seem to be related to the presence of peripheral events with a Carbon quasi-projectiles, since the velocity distribution of Carbon residues (shown in Figure 5) displays a good agreement with statistical calculations.

The angular distributions of protons and α particles in coincidence with each residue are shown in Figure 10. The good agreement among data and model predictions as far as proton distributions are concerned is confirmed. A large discrepancy is evident for α particles at backward laboratory angles detected in coincidence with an Oxygen fragment.

To understand the origin of the deviations from a statistical behaviour, the branching ratios to α decay and α kinematics in the different channels involving α emission will be studied in greater detail in Section 4.3.

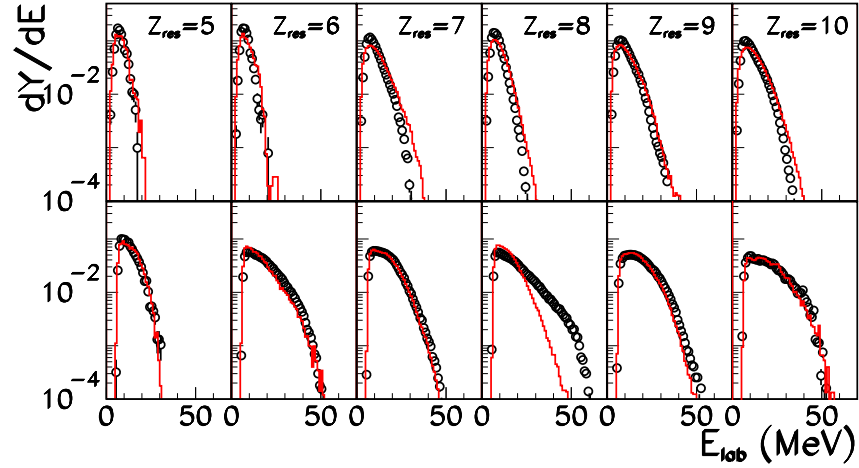


Figure 9. (Colour online) Proton (upper part) and α (lower part) laboratory energy spectra in complete events detected in coincidence with a residue of charge Z_{res} , indicated in each column. Data (symbols) are compared to model calculations (lines). All spectra are normalized to unitary area.

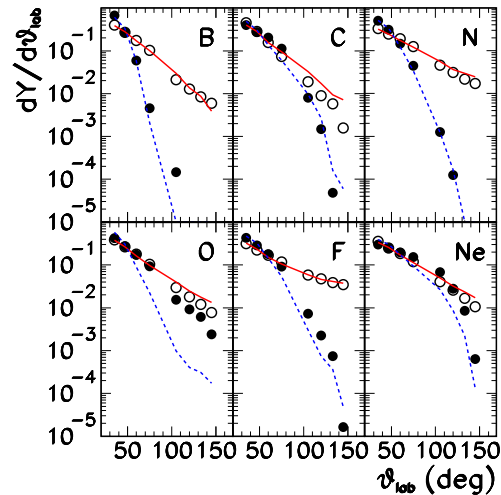


Figure 10. (Colour online) Proton (open symbols) and α (full symbols) angular distributions in the laboratory frame, detected in complete events in coincidence with the indicated residues. Data are compared to model calculations. Red solid lines correspond to protons, blue dashed lines to α 's. Experimental and calculated

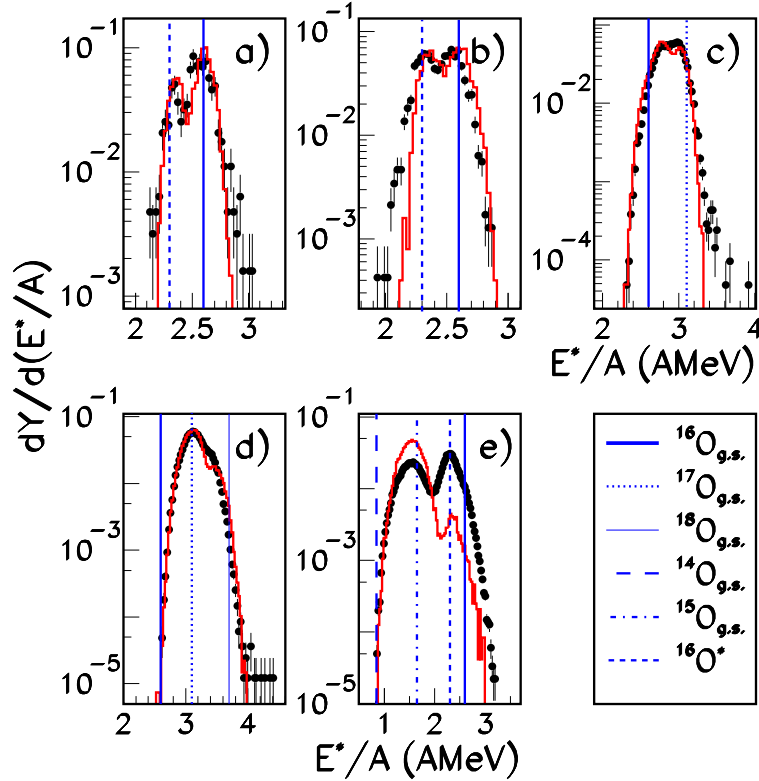


Figure 11. (Colour online) Calorimetric excitation energy distributions for the different channels associated with the production of an Oxygen residue: a) $\text{O}+\alpha+2\text{d}$; b) $\text{O}+\alpha+\text{p}+\text{t}$; c) $\text{O}+\alpha+\text{p}+\text{d}$; d) $\text{O}+\alpha+2\text{p}$; e) $\text{O}+2\alpha$. Full symbols: experimental data; (red) lines: HFℓ calculations. Blue vertical lines: expected values for the ground (excited) states of different isotopes, as listed in the bottom right panel. Data and calculations are normalized to unitary area.

4.2. Calorimetry and isotopic distributions

A deeper understanding of the reaction mechanism and a complementary test of the statistical behaviour can be obtained by studying the mass distribution of the different residues. Unfortunately we do not have isotopic resolution for fragments with atomic number $Z \geq 5$. However, if we consider in the analysis events completely detected in charge, the residue mass can be evaluated from the energy balance of the reaction, as we now explain.

Let us consider a well defined channel, characterized by a given residue charge Z_{res} , light charged particle charge $Z_{lcp} = 12 - Z_{res}$ and mass A_{lcp} . We define $\bar{Q} = m_{lcp}c^2 - m(^{24}\text{Mg})c^2$ the *partial* Q -value associated with that channel, where m_{lcp} is the total mass of the channel particles and $m(^{24}\text{Mg})$ is the mass of the composite nucleus. The unknown residue mass number A^k and unknown neutron number N^k in each event

k belonging to the considered channel are defined as a function of an integer isotopic variable x as $A_{res}(x) = 2Z_{res} + x$ and $N_n(x) = 24 - A_{lcp} - A_{res}(x) = 24 - A_{lcp} - 2Z_{res} - x$. The residue mass and total neutron energy are thus defined as a function of x : $m_{res}(x) = m(A_{res}(x), Z_{res})$, $E_n(x) = (\langle e_n \rangle + m_n c^2) N_n(x)$, where $\langle e_n \rangle$ is the estimate of the average neutron kinetic energy from the average measured proton one, with the subtraction of an average 2.9 MeV Coulomb barrier.

The excitation energy of the event k reads:

$$E_{theo}^* = \bar{Q} + m_{res}(x) + E_{kin}^k + E_n(x) + E_\gamma^k \quad (8)$$

where E_{kin}^k is the total measured kinetic energy, $E_{theo}^* = 62.4$ MeV the total available energy, and E_γ^k the unmeasured γ energy, in the centre of mass system. The excitation energy which would be associated to this event assuming that the residue has $A_{res} = 2Z_{res}$ and is produced in its ground state is:

$$E_{cal}(k) = \bar{Q} + m_{res}(x=0) + E_{kin}^k + E_n(x=0) \quad (9)$$

The example of Oxygen is reported in Figure 11. The calorimetric excitation energy distribution $E_{cal}(k)$ divided by the total mass of the system is displayed for the different measured channels associated to the production of $Z = 8$ fragments in complete events, together with the filtered model calculations. In all cases we can observe a wide distribution corresponding to different, often unresolved states of different isotopes. The qualitative agreement with the model calculations confirms once again that the selected events largely correspond to complete fusion.

In the hypothesis that the kinetic energies of LCP and neutrons depend on average on the channel, but not on the average value of the residue mass (through $\langle x \rangle$), (8) and (9) can be averaged over the events of the channel giving:

$$E_{theo}^* = \bar{Q} + m_{res}(x) + \langle E_{kin} \rangle + E_n(x) + \langle E_\gamma \rangle \quad (10)$$

$$\langle E_{cal} \rangle = \bar{Q} + m_{res}(x=0) + \langle E_{kin} \rangle + E_n(x=0) \quad (11)$$

Eqs. (10) and (11) allow for deducing the unmeasured neutron excess, and therefore the residue mass, from the average measured calorimetric energy. Indeed, subtracting the two equations we get:

$$\langle E_{cal} \rangle(x, I) = E_{theo}^* - (m_{res}(x) - m_{res}(x=0)) - (E_n(x) - E_n(x=0)) - E_I^* \quad (12)$$

This equation gives the calorimetric energy which is expected in average for a residue of mass number $A_{res} = 2Z_{res} + x$ produced in its excited state I , if we have assumed via (9) that its mass number is $2Z_{res}$, as shown for various cases by the blue vertical lines in Figure 11.

Our energy resolution is not sufficient to determine the detailed spectroscopy of each residue, but the comparison of the measured calorimetric energy in each event given by (9) with the expected value from (12) allows for a reasonably good isotopic identification.

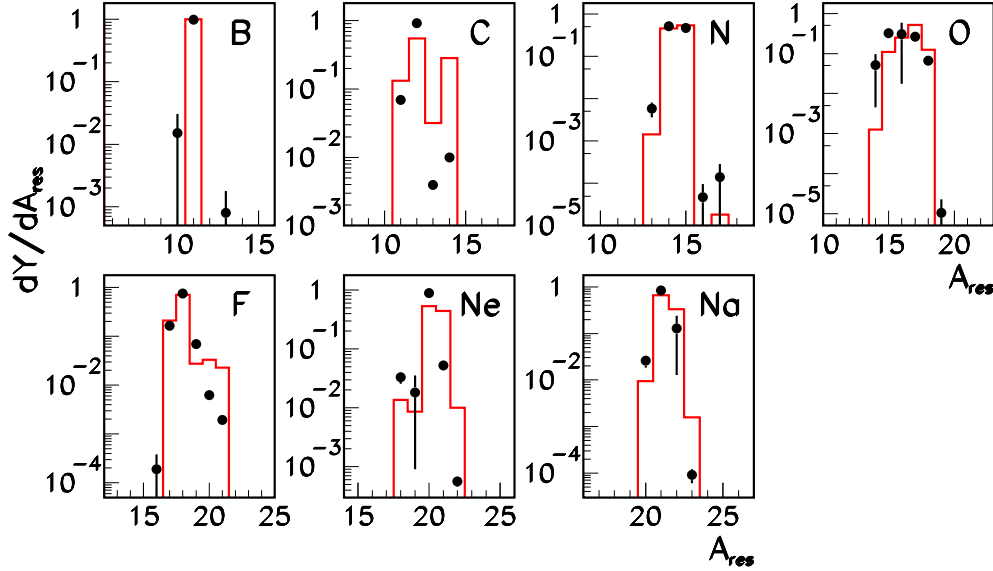


Figure 12. (Colour online) Experimental (symbols) isotopic distribution of residues obtained for complete events using (13) (see text), compared to theoretical predictions (histograms). Spectra are normalized to unitary area.

To attribute a definite isotope to each residue, we have minimized in each event k the distance in energy between the calorimetric result and the theoretical value associated to the resolved states of the associated channel

$$|E_{cal}(k) - \langle E_{cal} \rangle(x, I)| = \min \quad (13)$$

We have repeated the same procedure for all the residues. The resulting isotopic distributions are presented in Figure 12, again compared to the model calculations. Errors on experimental results have been obtained combining the statistical error with the one coming from the reconstruction procedure. This has been estimated by comparing, within the model, the values obtained by the reconstruction procedure with the original predictions. The global agreement is good, particularly for odd charge residues. Both the average and the width of the distributions are reproduced by the model. The distributions are generally bell-shaped and structureless, with the exception of Carbon, which shows an important depletion for ^{13}C similarly to the model calculation.

The case of Oxygen is particularly interesting. The experimental and theoretical widths are comparable, but while the experimental distribution has a negative skewness and it is centered on the neutron poor ^{15}O , the opposite is seen in the calculation which favours neutron rich isotopes and presents a positive skewness [17]. As we can see in Figure 11, this is largely due to the specific $O + 2\alpha$ channel. Indeed this channel is the

only one which leads to a non-negligible production of ^{15}O .

The information from the isotopic distribution and the energy spectra coherently points towards an increased probability for the $O + 2\alpha$ channel with respect to the statistical model. We therefore turn to see if the experimental sample contains, together with a dominant contribution of standard compound reactions, other reaction mechanisms which could selectively populate a few specific channels, possibly associated with α emission.

4.3. Multiple α channels

In Table 1 we report for each residue the most populated channel in the experimental sample, as well as the associated branching ratio. The results are compared to the prediction of the statistical model for the same channel, filtered through the characteristics of the experimental apparatus. We can see that the branching ratio of the dominant decay channels is reasonably well reproduced by the statistical model for odd- Z residues, while discrepancies can be seen for even- Z ones.

Z_{res}	channel	$BR_{HF\ell}$	BR_{EXP}
5	$^{11-xn}B+xn+p+3\alpha$	100%	99%
6	$^{12-xn}C+xn+3\alpha$	66%	98%
7	$^{15-xn}N+xn+p+2\alpha$	94%	91%
8	$^{16-xn}O+xn+2\alpha$	11%	63%
9	$^{19-xn}F+xn+p+\alpha$	87%	92%
10	$^{22-xn}Ne+xn+2p$	84%	55%

Table 1. For each measured residue, the table gives the most probable experimental channel and its branching ratio together with the value predicted by the HF ℓ calculations. Errors on the experimental values (about 5%) take into account both the statistical error and the possible $^3\text{He}-\alpha$ contamination.

For Oxygen, the predicted most probable channel is $^A\text{O}+\alpha+2H$ (here 2H stands for two $Z=1$ products) with a branching ratio $BR_{HF\ell} = 88\%$, while this channel is experimentally populated with $BR_{EXP} = 37\%$. For Carbon, $^{12}\text{C}+3\alpha$ is the most probable theoretical channel consistent with the data, but an important contribution of the channel $^{12}\text{C}+2\alpha+2H$ is also predicted ($BR_{HF\ell} = 32\%$), while this contribution is negligible in the experimental sample. Also for Neon a disagreement is present, but the theoretical calculation well reproduces the shape of the α spectrum, as shown in Figure 9. This is not the case for Oxygen and, to a lesser extent, Carbon. For these residues the discrepancy in the branching ratios affects the shape of the α particle spectra. This is shown in Figure 13, where, for the Carbon case (upper panels), the measured inclusive α spectrum is dominated by the multiple α channel, while in the statistical model the channel containing only two α particles (and hence two hydrogen

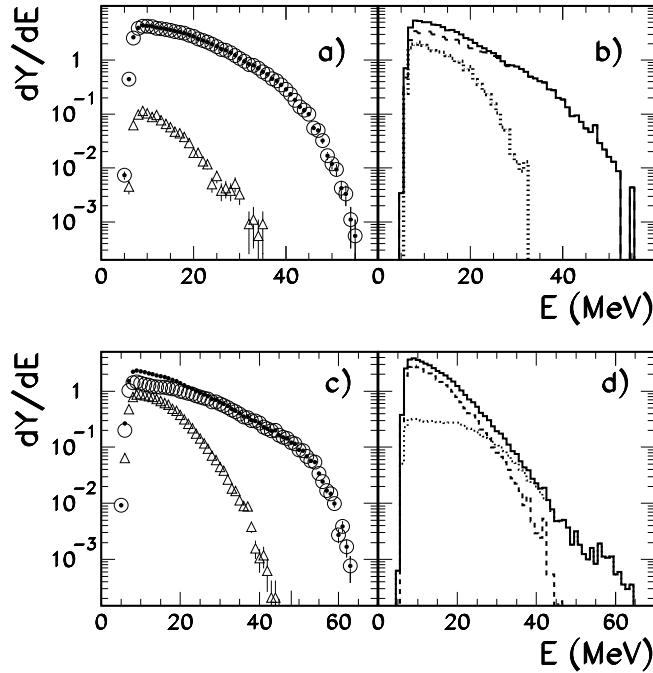


Figure 13. Experimental energy spectra (left) compared to HF ℓ calculations (right). Upper part: Carbon residue: full symbols and full line represent the inclusive distribution of all decay channels, open triangles and dashed line correspond to channels involving two α 's and two hydrogens, open circles and dotted line correspond to the three α 's channel. Lower part: Oxygen residue: Full symbols and full line represent the inclusive distribution of all decay channels, open triangles and dashed line correspond to $O + \alpha + 2H$ channel and open circles and dotted line correspond to $O + 2\alpha$ channel. The spectra are normalized to the number of events of each residue.

isotopes) is very important for low α energies, thus modifying the slope of the inclusive spectrum with respect to the data.

A similar analysis for Oxygen is presented in Figure 13 (lower panels). The same considerations as for Carbon apply in this case. Again, the extra yield associated with multiple α events with respect to the statistical model leads to a broader spectrum extending towards higher α energies.

If we now compare experimental data with model predictions in specific channels, we obtain, for the Carbon case (see Figure 14, upper panels), that the shape of the spectra of the different channels are very well reproduced by the statistical model calculations. The same holds true for the angular distributions, well reproduced by calculations. This shows that the kinematics of the decay is well described by a sequential evaporation mechanism. However these shapes depend on the channel, multiple α 's leading to spectra which are less steep and extend further in energy, with respect to channels

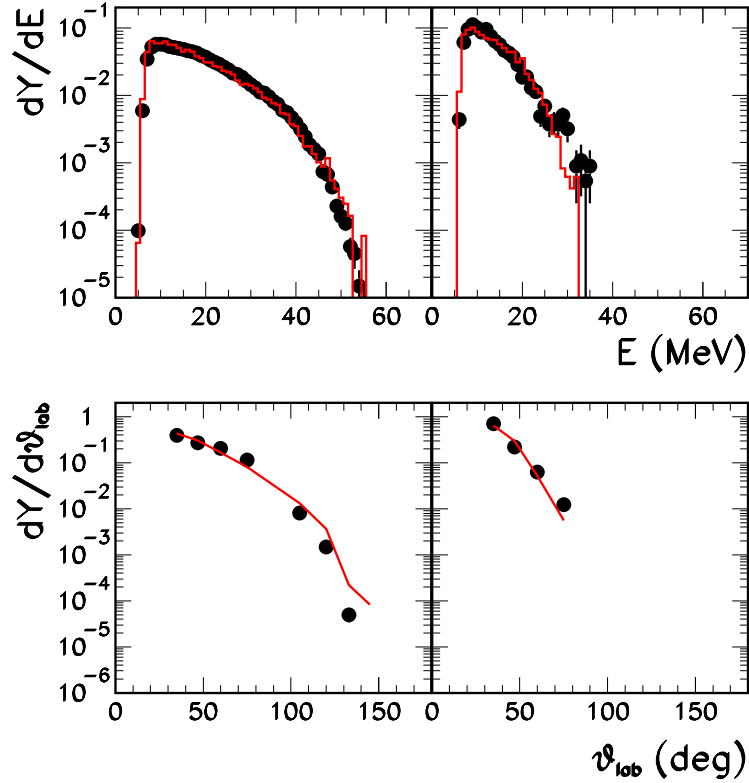


Figure 14. (Colour online) Energy spectra (upper panels) and angular distributions (lower panels) of α -particles detected in coincidence with a Carbon residue. Data (symbols) are compared to HF ℓ calculations (lines) for the two channels $C + 3\alpha$ (left) and $C + 2\alpha + 2H$ (right). All the spectra are normalized to unitary area in order to compare the shapes independently of the different branching ratios.

where hydrogens are also present. Because of that, the disagreement in branching ratios between model and data shown in Table I affects the global shape of the α spectrum, where the different channels are summed up.

Taking now into account the Oxygen residue, in Figure 15 we show the comparison of the energy spectra (upper panels) and angular distributions. At variance with the Carbon case, the shape of the α spectrum and the angular distribution in the $O + 2\alpha$ channel are not well reproduced by the statistical model. This means that the kinematics in this channel is not compatible with CN decay, and suggests a contamination from direct reactions.

The anomalously high probability of multiple α emission in coincidence with Oxygen and Carbon residues, with respect to the expectation from a statistical behaviour, can explain the deviations observed in the inclusive α observables (see Figures 6 and 7). This suggests that non-statistical processes are at play in the

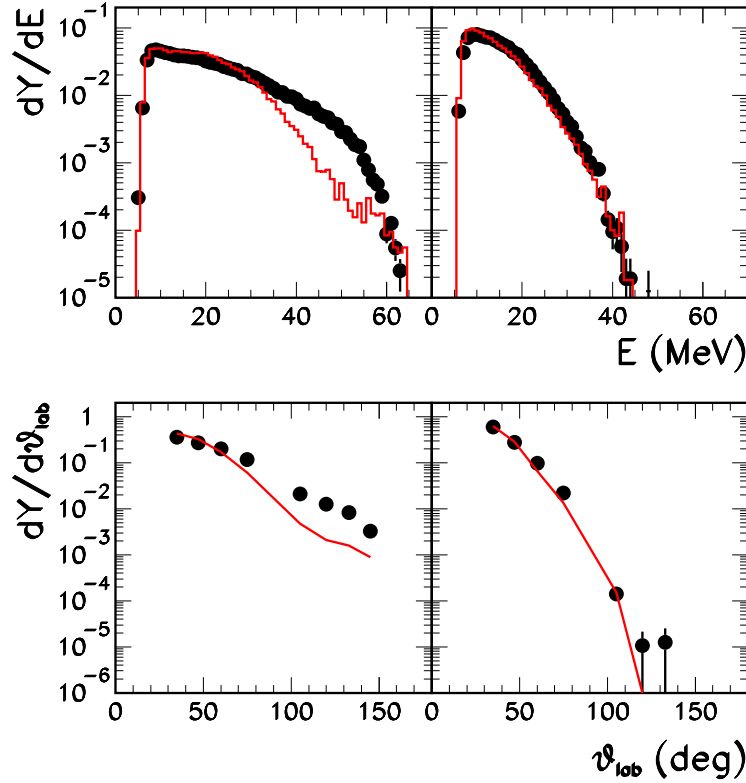


Figure 15. (Colour online) Energy spectra (upper panels) and angular distributions (lower panels) of α -particles detected in coincidence with an Oxygen residue. Data (symbols) are compared to HF ℓ calculations (lines) for the two channels $O + 2\alpha$ (left) and $O + \alpha + 2H$ (right). All the spectra are normalized to unitary area in order to compare the shapes independently of the different branching ratios.

experimental sample concerning the two specific multiple α channels that show anomalously high branching ratios.

Alpha production is known to be an important outcome of direct $^{12}\text{C}+^{12}\text{C}$ reactions [33, 34]. In these studies, though at lower bombarding energy than the present experiment, the α dominance has been associated with quasi-molecular two-Carbon excited states with a pronounced α structure.

In order to see if similar effects still persist at higher bombarding energies, in the second paper of the series we will focus on a detailed analysis of the multiple α channels.

5. Conclusions

In this work we have presented results for the $^{12}\text{C}(^{12}\text{C},\text{X})$ reaction at 95 MeV beam energy, measured at LNL-INFN with the GARFIELD+RCo experimental set-up.

Starting from a minimal selection of the fusion-evaporation mechanism, based on the coincidence between LCP's emitted over a wide polar angle range (GARFIELD) and a fragment detected at laboratory forward angles (RCo), reinforced by completeness conditions on the total detected charge and longitudinal momentum, we have compared experimental data to statistical model calculations for the decay of the $^{24}\text{Mg}^*$ CN issued in case of complete fusion.

The selected sample is compatible with the expected behaviour of a complete-fusion-evaporation reaction, with the exception of two specific channels significantly more populated than predicted by the HF ℓ calculations. These channels correspond to the emission of two or three α particles in coincidence with an Oxygen or Carbon residue, respectively. The α spectra and angular distributions in the $(O + 2\alpha)$ channel are not compatible with statistical model calculation. This suggests a contamination from direct reactions or α -structure correlations in the ^{24}Mg compound [35].

This is not the case for the $(C + 3\alpha)$ channel, and the anomalously high branching ratio of this channel can be tentatively attributed to a possible persistence at high excitation energy of α structure correlations in the $^{12}\text{C}+^{12}\text{C}$ molecular state and/or in the ^{24}Mg compound. The kinematic characteristics of these non-statistical decays are further studied in the continuation of this work [36].

The results of the analysis show that our data can be used to constrain the ingredients of the statistical model in the $A \leq 24$, $E^* \leq 2.6$ AMeV mass-excitation-energy region of interest.

In particular, this analysis supports a model showing a very steep increase of the level density with excitation energy. The value of the level density parameter around 3 AMeV excitation energy extracted from this study is consistent with early findings from fragmentation experiments.

Acknowledgments

The authors thank the crew of the XTU TANDEM acceleration system at LNL. This work was partially supported by the European Funds for Large Scale Facilities - Seventh Framework Program - ENSAR 262010 and by grants of Italian Ministry of Education, University and Research under contract PRIN 2010-2011.

References

- [1] Ghoshal S N 1950 *Phys. Rev.* **80** 939.
- [2] Alhassid Y, Bertsch G F and Fang L 2003 *Phys. Rev. C* **68** 044322; Nakada H and Alhassid Y, 2008 *Phys. Rev. C* **78** 051304(R); Alhassid Y *et al Preprint* nucl-th/13047258.
- [3] Guttormsen M *et al* 2003 *Phys. Rev. C* **68** 064306; Nyhus H T *et al* 2012 *Phys. Rev. C* **85** 014323.
- [4] Charity R *et al* 2003 *Phys. Rev. C* **67** 044611; Charity R J 2010 *Phys. Rev. C* **82** 014610.
- [5] Canto L F *et al* 2006 *Phys. Rep.* **424** 1, and references therein.
- [6] Adhikari S *et al* 2006 *Phys. Rev. C* **74** 024602.
- [7] Von Egidy T and Bucurescu D 2005 *Phys. Rev. C* **72** 044311; Von Egidy T and Bucurescu D 2006 *Phys. Rev. C* **73** 044601.

- [8] Wiringa R B, Pieper S C, Carlson J and Pandharipande V R 2000 *Phys. Rev. C* **62** 014001; Kanada-Enyo Y and Horiuchi H 2001 *Prog. Theor. Phys. Suppl.* **142** 205; Neff T and Feldmeier H 2004 *Nucl. Phys. A* **738** 357.
- [9] Ikeda K, Tagikawa N and Horiuchi H 1968 *Prog. Theor. Phys. Extra Suppl. (Jpn)* 464; Horiuchi H, Ikeda K and Kato K 2012 *Prog. Theor. Phys. Suppl.* **192** 1.
- [10] J. A. Maruhn J A, M. Kimura M, S. Schramm S, P.-G. Reinhard P-G, H. Horiuchi H and A. Tohsaki A 2006 *Phys. Rev. C* **74** 044311; Reinhard P G, Maruhn J A, Umar A S and Oberacker V E 2011 *Phys. Rev. C* **83** 034312.
- [11] Ebran J P, Khan E, Niksic T, Vretenar D 2012 *Nature* **487** 341-344.
- [12] Matsumura H and Suzuki Y 2001 *Nucl. Phys. A* **739** 238; Yamada T and Schuck P 2004 *Phys. Rev. C* **69** 024309.
- [13] Freer M 2007 *Rep. on Prog. in Phys.* **70** 2149.
- [14] Costanzo E *et al* 1991 *Phys. Rev. C* **44** 111; Grenier F *et al* 2008 *Nucl. Phys. A* **811** 233; Raduta A R *et al* 2011 *Phys. Lett. B* **705** 65-70; Kokalova Tz, Itagaki N, von Oertzen W and Wheldon C 2006 *Phys. Rev. Lett.* **96** 192502; von Oertzen W *et al* 2008 *Eur. Phys. Journ. A* **36** 279; Di Pietro A *et al* *Journal of Physics: Conference Series* **366** 012013; Vardaci E *et al* 2013 *Journal of Physics: Conference Series* **436** 012054 and references quoted therein.
- [15] Wallner A, Strohmeier B and Vonach H 1995 *Phys. Rev. C* **51**, 614.
- [16] Baiocco G 2012 *PhD Thesis, Università di Bologna and Université de Caen Basse-Normandie*
<http://amsdottorato.cib.unibo.it/4295/>
- [17] Baiocco G *et al* 2013 *Phys. Rev. C* **87** 054614.
- [18] Hauser W and Feshbach H 1952 *Phys. Rev.* **87** 366.
- [19] Chen Z and Gelbke C K 1988 *Phys. Rev. C* **38** 2630.
- [20] <http://www.chemistry.wustl.edu/rc/gemini++/>
- [21] <http://www.nndc.bnl.gov/amdc/>
- [22] <http://www.nndc.bnl.gov/nudat2/>
- [23] Ignatyuk A V *et al* 1975 *Sov. J. Nucl. Phys.* **21** 255; Iljinov A S *et al* 1979 *Nucl. Phys. A* **543** 450.
- [24] Toke J and Swiatecki W J 1981 *Nucl. Phys. A* **372** 141.
- [25] Ricciardi M V *et al* 2004 *Nucl. Phys. A* **733** 299.
- [26] Gramegna F *et al* *Nucl. Instrum. Methods A* **389** 474; Gramegna F *et al* 2004 *IEEE Nucl. Science Symposium, Rome IEEE Nucl. Sci. Symp. Conf. Proc.* **2** 1132; Moroni A *et al* 2006 *Nucl. Instrum. Methods A* **556** 516.
- [27] Bruno M *et al* 2013 *Eur. Phys. Journ. A* **42** 128.
- [28] Morelli L *et al* 2010 *Nucl. Instrum. Methods A* **620** 305.
- [29] Rivet M F (*INDRA collaboration*) and De Filippo E (*CHIMERA collaboration*) - private communications.
- [30] Bardelli L *et al* 2011 *Nucl. Instrum. Methods A* **654** 272; Carboni S *et al* 2012 *Nucl. Instrum. Methods A* **664** 251.
- [31] Tarasov O. B. and Bazin D 2003 *Nucl. Instrum. Methods B* **204** 174.
- [32] Gomez del Campo J *et al* 1979 *Phys. Rev. C* **19** 2170; Parks R L *et al* 1980 *Nucl. Phys. A* **348** 350; Kovar G *et al* 1979 *Phys. Rev. C* **20** 1305; Sperr P *et al* 1976 *Phys. Rev. Lett.* **37** 321; Nambodiri M N *et al* 1976 *Nucl. Phys. A* **263** 491.
- [33] Cosman E R *et al* 1975 *Phys. Rev. Lett.* **35** 265; Bremner C A *et al* 2002 *Phys. Rev. C* **66** 034605; Cormier T M, Jachcinski C M, Berkowitz G M, Braun-Munzinger P, Cormier P M, Gai M, Harris J W, Barrette J and Wegner H E 1978 *Phys. Rev. Lett.* **40** 924; Morsad A, Haas F, Beck C and Freeman R M 1991 *Z. Phys. A* **338** 61.
- [34] Wuosmaa A H *et al* 1992 *Phys. Rev. Lett.* **68** 1295; Aliotta M *et al* 1995 *Z. Phys. A* **353** 43; Le Marechal R A *et al* 1997 *Phys. Rev. C* **55** 1881.
- [35] Morelli L *et al* *Preprint nucl-ex/1309.0323 - Contribution to the 25th International Nuclear Physics Conference (INPC 2013), Firenze, Italy.*
- [36] Morelli L *et al* submitted to *J. Phys. G: Nucl. Part. Phys.* .